Tuesday, 31 July, 2012

Rapid radiation belt losses occurring during high speed solar wind stream driven storms: importance of energetic electron precipitation

Aaron T. Hendry and Craig J. Rodger

Department of Physics, University of Otago, Dunedin, New Zealand

Mark A. Clilverd

British Antarctic Survey (NERC), Cambridge, United Kingdom

Neil R. Thomson

Department of Physics, University of Otago, Dunedin, New Zealand

Steven K. Morley

Los Alamos National Laboratory, Los Alamos, New Mexico, USA

Tero Raita

Sodankylä Geophysical Observatory, University of Oulu, Sodankylä, Finland

Abstract. Recent studies have shown how trapped energetic radiation belt electron fluxes rapidly "drop out" during small geomagnetic disturbances triggered by the arrival of a Solar Wind Stream Interface (SWSI). In the current study we use satellite and ground-based observations to describe the significance of energetic electron precipitation (EEP) and direct magnetopause shadowing loss mechanisms, both of which have been suggested as possible causes of the dropouts. Superposed epoch analysis of low-Earth orbiting POES spacecraft observations indicate that neither "classic" magnetopause shadowing or EEP appear able to explain the dropouts. However, SWSI-triggered dropouts in trapped flux are followed ~3 hours later by large increases of EEP, which start as the trapped electron fluxes begin to recover, and may be signatures of the acceleration process which rebuilds the trapped fluxes. Ground based observations indicate typical >30 keV EEP flux magnitudes of ~8×10^5

electrons cm^{-2} sr^{-1} s^{-1}. While these are ~10 times larger than the equivalent precipitating fluxes measured by POES, that is consistent with the small viewing window of the POES telescopes.

1. Introduction

The basic structure of the Van Allen radiation belts was recognized from shortly after their discovery following the International Geophysical Year [*Van Allen and Frank*, 1959; *Hess*, 1968]. Despite being discovered at the dawn of the space age, there are still fundamental questions concerning the acceleration and loss of highly energetic radiation belt electrons [*Thorne et al.*, 2010]; energetic electron fluxes can increase or decrease by several orders of magnitude on time scales of less than a day. The coupling of the Van Allen radiation belts to the Earth's atmosphere through precipitating particles is an area of intense scientific interest, principally due to two differing research activities. One of these concerns the physics of the radiation belts, and primarily the evolution of energetic electron fluxes during and after geomagnetic storms [e.g., *Reeves et al.,* 2003]. The other focuses on the response of the atmosphere to precipitating particles, with a possible linkage to climate variability [e.g., *Turunen et al*., 2009*; Seppalä et al.,* 2009]. Both scientific areas require increased understanding of the nature of the precipitation, particularly as to the precipitation drivers, as well as the variation of the fluxes and energy spectrum for electrons lost from the outer radiation belts. One area of interest has been the link between the weak geomagnetic storms triggered by the arrival of a high speed solar wind stream interface (SWSI) and associated "dropouts" in energetic electron fluxes [e.g., *O'Brien et al.*, 2001; *Miyoshi and Kataoka*, 2008; *Morley et al.*, 2010a]. These events highlight the dynamic nature of the outer radiation belt electron fluxes, and are the subject of a review in the current monograph [*Turner et al.*, 2012].

The combination of observations from a large number of spacecraft provides a much higher time resolution than possible from single spacecraft, and this has recently provided new understanding into the SWSI-linked dropout events. A statistical study utilizing 9 GPS-borne particle detectors and superposed epoch analysis around the arrival of 67 SWSIs showed a strong repeatable "signal" of a rapid electron flux dropout [*Morley et al.,* 2010b]. Dropouts occurred in a median time scale of ~7 h, with median electron counts falling by 0.4–1.8 orders of magnitude for all *L** (where L* is a magnetic drift invariant [*Roederer*, 1970]). The SWSI triggered geomagnetic storms with small Dst excursions (-40 nT) and small Kp increases (Kp≈4). Indeed, while these events show a storm-like evolution in Dst and Kp, the majority have maximum Dst excursions less than -30 nT and thus are not storms by the "traditional" definitions [e. g., *Loewe and Prölss*, 1997], although we will refer to them as such for want of a better label. The storms started ~6 hours before the epoch defined by the expected arrival of the SWSI at the Earth's bow shock nose. While the radiation belt dropouts and recoveries depended on both *L** and energy, only three of 67 SWSIs did not have an associated dropout in the electron data.

In the current study we reconsider satellite and ground-based observations to describe the significance of energetic electron precipitation during SWSI-driven geomagnetic storms. We make use of the *Morley et al.* [2010b] epochs to allow 'like with like' comparisons with the earlier GPS study. Here we show that the EEP occurs well after the dropout has started, and confirm the EEP energy dependence reported earlier. From the existing literature it appears possible that the dropout is caused by magnetopause shadowing. However, this study shows that the SWSI also triggers a geomagnetic storm some hours after the dropout which enhances wave-particle interactions leading to EEP, as well as the recovery and enhancement of the trapped electron fluxes. We go on to use ground-based EEP observations to determine the likely precipitation flux into the atmosphere. SWSI-driven events are highly repeatable in form, and lead to order of magnitude enhancements in EEP up to very high *L*-shells. As such the EEP will couple efficiently into the polar vortex, and may influence the chemistry and dynamics of the polar neutral atmosphere. Recent work has demonstrated that geomagnetic storms produce levels of EEP that are significant in the lower ionosphere [e.g., *Rodger et al.*, 2007], and can significantly alter mesospheric neutral chemistry [*Newnham et al.*, 2011].

2. POES observations

2.1 SWSI Event Epochs

As noted above we make use of the epochs given by *Morley et al.* [Table A.1, 2010b]. The experimental data we use in this study, POES electron counts and subionospheric VLF propagation, are both strongly affected by high energy protons which are likely to dominate over any electron response. We therefore removed two of the Morley epochs (7 May 2005 and 28 July 2005) from our list as these occurred in the declining phase of solar proton events. We therefore have 65 epochs in total from Table 2 of Morley et al. [2010b].

In our investigation of the POES spacecraft data described below we follow the approach of earlier authors and undertake superposed epoch analysis (SEA). We explicitly follow the approach of *Morley et al.* [2010b].

2.2 POES SEM-2 Observations

We make use of measurements from the Space Environment Monitor (SEM-2) instrument package onboard the Polar Orbiting Environmental Satellites (POES) which are in Sun-synchronous orbits at ~800-850 km altitudes. SEM-2 includes the Medium Energy Proton and Electron Detector (MEPED). For a detailed description of the SEM-2 instruments, see *Evans and Greer* [2004]. We use SEM-2 observations from the NOAA-15 through 19 satellites plus the METOP-2 satellite which also carries an SEM-2. All POES data is available from http://poes.ngdc.noaa.gov/data/ with the full-resolution data having 2-s time resolution. NOAA has developed new techniques to remove the significant low-energy proton contamination from the POES SEM-2 electron observations [e.g., *Rodger et al.*, 2010a], which has been described in Appendix A of *Lam et al.* [2010]. This algorithm is available for download through the Virtual Radiation Belt Observatory (ViRBO; http://virbo.org).

The SEM-2 detectors include integral electron telescopes with energies of >30 keV (e1), >100 keV (e2), and >300 keV (e3), pointed in two directions. Modeling work has established that the 0° telescopes monitor particles in the atmospheric bounce loss cone that will enter the Earth's atmosphere below the satellite when the spacecraft is poleward of *L*<1.5-1.6 [*Rodger et al.*, Appendix A, 2010b]. Note however, that the 0° telescopes only observe a fraction of the bounce loss cone even when they are directed such that they only measure bounce loss cone fluxes; building on the *Rodger et al.* [2010b] modeling we find that in practice at best 10% of the total bounce loss cone area is sampled, a value which can drop to less than ~2.5% depending on the location. In contrast the 90º directed MEPED-telescope tends to detect electrons with higher pitch angles, i.e. the drift loss cone and trapped electron populations. In practice, once even a small fraction of trapped electron fluxes are visible to the instrument these will strongly dominate over any fluxes inside a loss cone. This occurs from roughly *L*=4-5 and above, depending on the location.

In addition to the electron telescopes, the MEPED instrument also includes a number of proton telescopes. The SEM-2 proton detectors also suffer from contamination, falsely responding to electrons with relativistic energies which can be useful for radiation belt studies [e.g., *Sandanger et al.*, 2007; *Yando et al.*, 2011] outside of solar proton events when significant energetic proton fluxes are present. In particular the P6 telescope detectors, which are designed to measure >6.9 MeV protons, also respond to either trapped or bounce loss electrons (depending on *L*-shell) with energies in the relativistic range [*Yando et al.*, 2011]. As shown in Figure 8 of *Yando et al*. [2011], the P6 channel plays a complementary role to the e1–e3 channels for detection of relativistic electrons, and is sensitive to electrons of energy larger than roughly 1000 keV.

2.3 Superposed Epoch Analysis of MEPED electrons

Before undertaking superposed epoch analysis we first combine the POES reported particle fluxes varying with *L* and time, using 0.25-*L* and 1-hour time resolution. Observations from inside and around the South Atlantic Magnetic Anomaly are excluded before the measurements are combined. From this dataset superposed epoch analysis is undertaken using the 65 epochs from *Morley et al.* [2010b]; in addition, another superposed epoch analysis is undertaken with a set of 65 epochs which are randomly selected from the period January 2004 to December 2008, after having been filtered for solar proton events. This allows an additional check of the significance of any changes observed in the Morley epoch superposed epoch analysis.

2.3.1 POES observations of trapped flux changes

Figure 1 shows the results of this analysis on the 90º directed telescopes, i.e. those primarily showing the effect of SWSI on trapped fluxes. The left hand panels show the results of analysis using the Morley epochs, while the right hand side are for the random epochs. The upper panels are the integral flux observations from the >100 keV 90º telescope, the middle panels show the relativistic electron flux variation from the P6 90º telescope, and the lower panels the differential proton flux at 346 keV from the P3 90º telescope.

As a guide, all of the left hand panels include the result of the superposed epoch analysis applied to GOES >600 keV trapped flux observations for the Morley epochs (green line). The superposed epoch analysis of the >600 keV trapped electrons from geostationary orbits at *L*≈6.6 shows a very similar timing to the dropouts in trapped electron fluxes from the GPS spacecraft, which were also made near the geomagnetic equator (i.e. around geostationary orbit). The GOES superposed epoch analysis has been scaled and shifted to fit on this plot, but involves a flux drop of ~1.5 orders of magnitude, with a recovery to a flux level that is ~50% larger than the initial levels. The rapid dropout starts at -0.7 day (relative to the epoch time), reaching the deepest point at +0.2 day, with the fluxes having returned to the same level by about +1 day.

The POES data shown in Figure 1 indicates that the observations of the trapped electrons and protons near the bottom of the geomagnetic field lines are very different from that near the geomagnetic equator, and different from one another. While there is some evidence for a dropout in the >100 keV electrons, this is only true for *L* greater than about 6 and starts just around the zero epoch. The >300 keV 90º electron fluxes also include some evidence of a dropout (from *L* greater than about 5.5; not shown, although similar plots have been produced by *Miyoshi and Kataoka* [Fig. 3, 2008]); while the >30 keV 90º do not show a clear dropout (not shown). The relativistic electron observations provided by the P6 90º telescope do show a dropout, but this seems to start well after the dropout occurring near the geomagnetic equator. In contrast to all of the electron observations, the trapped differential 346 keV proton fluxes from P3 increase around the time the dropout begins in the electron fluxes near the geomagnetic equator. The same behavior is seen in the 90º-directed P1, P2, and P4 detectors (not shown). The significance of the variation shown in the left-hand panels is particularly clear when contrasted for the random epoch SEA results presented in the right hand panels.

In order to clarify the differences between the electron responses, Figure 2 presents line plots of the changing 90º electron observations from the >100 keV and P6 telescopes at *L*=5.4. Following the format of *Morley et al.* [2010b], we show the superposed epoch median of the quantity by a black line. The 95% confidence interval for the median is given by the dark grey band. The inner bands mark the interquartile range (medium grey) and the 95% confidence interval about it (light grey). Figure 2 demonstrates the strong differences between the responses of the >100 keV electrons and the relativistic electrons from the P6 channel. During the quiet period before the start of the SWSI-triggered geomagnetic storm, the >100 keV trapped electron fluxes steadily drop. This is reversed at the zero epoch, very close to the time when the electron flux dropouts observed near the geomagnetic equator by GOES and GPS reach their "deepest" extent. In contrast to the >100 keV trapped fluxes, the relativistic electrons exhibit a well-defined dropout which starts around the same time as seen in the GOES superposed epoch analysis, recovers after 1-1.5 days, and climbs to a slightly higher flux level.

2.3.2 POES observations of precipitating flux changes

Figure 3 shows superposed epoch analysis applied to two of the 0º-directed telescopes, i.e. those telescopes which detect a portion of the electrons which precipitate into the atmosphere. The format of Figure 3 is otherwise the same as Figure 1. The top panels of this figure show the variation of the >100 keV 0º telescope. By comparison with the random epoch analysis shown on the right-hand side, it is apparent that 4-5 days before the SWSI arrives the magnitude of >100 keV precipitation is "normal", and then steadily decreases by ~0.5 order. This is likely to be linked to the "calm before the storm", intervals of unusually calm geomagnetic activity, which have been previously reported [e.g. *Clilverd et al.*, 1993]. Very shortly before the zero epoch the >100 keV flux begins to increase by nearly 2 orders of magnitude (but only slightly more than 1 order of magnitude larger than normal conditions). This peak of precipitation is ~+0.3 days after the zero epoch, around the time the GPS and GOES observed electrons dropouts are at their deepest. The most significant EEP stretches from L=5 to L=8.5, although there is a clear increase to at least L=14. The EEP decays slowly over the 5 days after the epoch to roughly normal levels. Similar patterns occur with the >30 keV and >300 keV EEP (not shown; *Meredith et al.*, Fig.1, 2011]. In contrast, however, the relativistic electron flux from the 0º P6 telescope does not display a decrease before the SWSI arrives (i.e., no "calm" in relativistic EEP), and exhibits a small decrease in precipitation magnitude during the peak timing of the >100 keV EEP, lasting perhaps 1-2 days.

3. Consistency with loss mechanisms

As noted in the introduction, the existing literature has identified three possible causal mechanisms to explain the GPS-observed dropout in trapped electron fluxes 1) magnetopause shadowing, 2) EEP into the atmosphere due to wave-particle interactions, and 3) outward diffusion through the magnetopause. The POES superposed epoch analysis described in the previous section allows us to make conclusions as to the validity of the first two of these loss mechanisms. Note that the monograph in which this paper appears also contains a review covering the major loss mechanisms associated with dropouts [*Turner at al.*, 2012].

3.1 Mechanism 1: Magnetopause Shadowing

As previously noted by *Morley et al.* [2010a], our existing understanding is that the loss timescales possible from the EEP or outward diffusion are not fast enough to explain the dropouts as observed. As such, magnetopause shadowing, sometimes termed "magnetopause encounters" may appear the more likely candidate. This mechanism involves radiation belt particles drifting around the Earth, encountering the magnetopause boundary and being swept away by the solar wind and permanently lost. Characteristics of particle losses by magnetopause shadowing are 1) pitch angle independence of losses of particles on a given drift shell, such that losses would be expected for both high pitch angle particles which spend most of their time near the geomagnetic equator and low pitch angle particles which mirror near to the top of the atmosphere; 2) independence of particle charge, mass or energy, such that electrons or protons which are drifting around the Earth on the same L-shell (but in opposite directions) will encounter the magnetopause and hence be lost.

On this basis one would expect the dropouts of electrons observed in the trapped electron fluxes near the geomagnetic equator by the GPS spacecraft to also be seen in both the trapped electron and proton fluxes measured by the POES low-Earth orbiting spacecraft. As reported in Section 2.3.1, neither of these conditions hold, as the >30 and >100 keV trapped electron fluxes do not show the dropouts reported by satellites near the geomagnetic equator. In addition, the trapped proton fluxes increase rather than decrease during the dropouts. This suggests that direct magnetopause encounters cannot be used to explain the electron flux dropouts. Note that a similar argument was previously employed by *Green et al.* [2004] who contrasted the observed losses of protons and electrons to exclude magnetopause encounters as the dominant loss mechanism.

3.2 Mechanism 2: EEP into the Atmosphere

As shown in Figures 3 and discussed in Section 2 above, the >30, >100 and >300 keV 0º electron telescopes (which measure part of the bounce loss cone) do show significant increases in EEP, but starting at the point that the dropout is at its deepest point and beginning to recover. In contrast, the relativistic electron fluxes measured by the P6 0º telescope show a small decrease in EEP at the same time. Clearly, these observations are not consistent with EEP as the primary mechanism to explain the dropouts. Indeed, it is possible that the opposite is true, that the EEP is the signature of wave-particle driven acceleration processes which serve to reverse the electron flux dropouts [e.g., *Thorne*, 2010, and references within].

4. AARDDVARK observations

Subionospheric VLF propagation detects precipitation due to changes in the ionization number density at altitudes around the lower D-region boundary. As the VLF waves propagate beneath the ionosphere in the Earth-ionosphere waveguide the EEP-induced ionization produces changes in the received amplitude and phase. Due to the low attenuation of VLF subionospheric propagation, the EEP modified ionospheric region may be far from the transmitter or the receiver. As the received subionospheric amplitude is the sum of multiple propagation modes, the response to changes in the waveguide is often complex, and both increases and decreases in amplitude are possible when increased ionization occurs in the waveguide (see for example, Fig. 4 of *Rodger et al.* [2012]). The response also depends on the solar zenith angle along the path. As a result of these factors subionospheric VLF is not particularly suitable for analysis through superposed epoch. We have, therefore, checked individual paths for a set of specific events to confirm the occurrence of significant EEP.

In this study we make use of narrow-band subionospheric VLF data received at Churchill (CHUR, 58.75ºN, 265.1ºE, *L*=7.6) and Sodankylä, Finland (SGO, 67.4ºN, 26.4ºE, *L*=5.3). Both these receivers are part of the Antarctic-Arctic Radiation-belt Dynamic Deposition VLF Atmospheric Research Konsortia (AARDDVARK) [*Clilverd et al.*, 2009]. While the AARDDVARK observations have sub-second time resolution, we will restrict ourselves to 1-minute median values to describe the overall transmitter operations. Figure 4 shows the transmitter-receiver Great Circle Paths (GCP) which have been monitored by the Churchill and Sodankylä receivers for at least some part of the time period considered.

The AARDDVARK data was manually examined for evidence of EEP around the time of the Morley epochs. The process was as follows: for each Morley epoch, AARDDVARK data plots were made for all the transmitters monitored by the Churchill and Sodankylä receivers. Data for four days both before and after the epoch day were plotted. The days before the epoch were included primarily to construct a Quiet Day Curve (QDC) to provide comparisons with the epoch day. POES observations show that EEP levels are low immediately before the SWSI epoch, which should allow a good AARDDVARK QDC to contrast with the epoch day. Figure 5 shows examples of the data examined in this way. The upper panel of this figure presents the received amplitude of the GVT 22.1 kHz transmitter received at Sodankylä (2.5< *L* <5.3) around the Morley epoch at 6:30 UT on 28 May 2008. Observations on the days before the epoch day are plotted in grey, the epoch day in black. At this time of year most of the GVT-SGO GCP is sunlit throughout the day, although the transmitter-end of the path will have a nighttime ionosphere from ~20-04 UT. In general, subionospheric VLF propagation is more sensitive to EEP for nighttime rather than daytime ionospheric conditions [*Rodger et al.*, 2012], due to the extremely large D-region energy input from the Sun during the day. On this day there is a very clear precipitation-induced decrease in the received amplitude starting about 1 hour after the epoch (the epoch being marked by the vertical line) continuing through to ~11 UT where the amplitude clearly returns to the QDC defined by the previous days. In this time the amplitude initially decreases by ~1.3 dB, after which it returns to near QDC levels. In the hours following there are several subsequent examples of likely precipitation periods (i.e., ~13.5 UT and 15.5 UT), both of which have quite small amplitude changes in comparison with the first precipitation period.

The lower panel of Figure 5 presents the received amplitude of the NDK 25.2 kHz transmitter received at Churchill (2.8< L <7.4) around the Morley epoch at 14:00 UT on 22 July 2008. Once again, there is a long period when the entire path is sunlit, from ~12-2UT. Unfortunately, the transmitter was not operating for a few hours around the time of the epoch. However, the amplitude on the event day is well behaved from ~2 hours after the epoch, showing a steady rise from 15.5-20.75 UT, followed by three broad bursts of precipitation at 21.5 UT, 23 UT, and 0.25 UT on the following day.

Of the 65 Morley epochs that we studied, there were 7 epochs for which there were no Sodankylä AARDDVARK observations either on the epoch day, or on one of the days immediately before the epoch, leaving 58 epochs to examine. The Churchill AARDDVARK receiver was not installed until May 2007, halfway through the period containing the Morley epochs, and was also not operating from December 2007 through May 2008. As a result, only 14 epochs were able to be examined in the Churchill data, although most of these epochs are also represented in Sodankylä observations. We classified data as showing evidence of EEP if an obvious deviation from the QDC could be seen concurrently on at least two different transmitter-receiver paths; this was to ensure the deviations we were seeing were indeed due to EEP, and not through random fluctuations in the AARDDVARK data.

We performed the above analysis on both the aforementioned Morley epochs. For the 67 Morley epochs, 2 epochs were removed due to solar proton activity, 4 were removed as neither receiver was operating, and 15 epochs were removed as there was no transmitter-receiver path with a good QDC. Of the remaining 46 epochs, 34 of these showed clear signs of EEP across multiple paths (i.e., 74%). This confirms the riometer and satellite-based observations of significant EEP occurring during the SWSI dropouts, and also provides us with an additional dataset in order to determine the magnitude of the EEP entering the atmosphere.

5. AARDDVARK modeling

For the next step, we returned to the Morley epochs, focusing on the paths which had a well-behaved QDC, again concentrating on times when the path is sunlit. We then focused on only three subionospheric transmitter-receiver paths; NAA 24.0 kHz to Churchill and GVT to Sodankylä, both of which are relatively short paths which span a limited MLT range, and the rather long path from NAA to Sodankylä. There is a significant amount of variability in the observed amplitude changes; this is hardly surprising given the large variability in the magnitude of the EEP from event to event evidenced from the interquartile range (not shown). However, we are still in a position to establish "typical" amplitude changes for the subionospheric VLF observed SWSI-associated precipitation. These are shown in Table 1.

In order to determine the typical magnitude of the EEP triggered by the SWSI, we follow the modeling approach outlined in *Rodger et al.* [2012]. Here our goal is determine the fluxes which will lead to the changes in VLF amplitude shown in Table 1. In addition, *Morley et al.* [2010b] reported that the SWSI-associated radiation belt dropouts were linked to increases in riometer-measured absorption of "cosmic noise", which is expected due to increases in the ionization number density in the ionospheric D- and E-regions caused by EEP. A SEA analysis of riometer data found that the change in cosmic noise absorption (ΔCNA) in Canadian and European instruments peaked at ~1.25 dB in the period 3-6 hours following the epoch [*Morley et al.*, 2010b]. Thus our modeling goal is reproduce both the subionospheric VLF changes as well as those from the riometer SEA.

For each VLF transmitter-receiver path we take a modeling point midway along the path, and use a combination of International Reference Ionosphere (IRI-2007) [online from http://omniweb.gsfc.nasa.gov/vitmo/iri_vitmo.html] and typical D-region electron density profiles determined for high latitudes at noon [*Thomson et al.*, 2011]. We model the SWSI-associated EEP signature in ground-based data using 10 keV-2.0 MeV precipitating electrons with an energy spectra determined by the POES SEA observations. During the peak precipitation period, the >30, >100 and >300 keV precipitating fluxes are best fitted terms of a power law where the slope (scaling exponent, *k*) is -3.5. Otherwise our modeling techniques follow that described by *Rodger et al.* [2012].

As shown in Table 1, a relatively small range of EEP flux magnitudes will reproduce the ground-based instrument responses observed during the SWSI-triggered geomagnetic storms. The top half of the table examines the EEP values necessary to best reproduce the subionospheric VLF amplitude change observations (ΔVLF obs.), and shows the predicted change in riometers absorption (ΔCNA calc.) predicted for that EEP flux striking the atmosphere at the midpoint of that path. Although the lower bound of the EEP was assumed to be 10 keV (to more accurately capture the riometers responses), we report the >30 keV EEP flux magnitude to allow direct comparison with the POES 0º-telescope observations, given below. Table 1 shows there is very good agreement between the modeled and predicted VLF responses (ΔVLF calc.) for the paths NAA-CHUR and NAA-SGO with >30 keV EEP flux magnitudes of 9-10×10^5 electrons cm^{-2} sr^{-1} s^{-1}, and slightly lower quality matching for the GVT-SGO path, where -1.1 dB is the largest negative amplitude change we can produce (c.f., a typical change of -1.5 dB observed) for a >30 keV EEP flux magnitude of 4×10^5 electrons cm^{-2} sr^{-1} s^{-1}. These EEP are calculated to produce riometer absorption changes which are similar to those reported (1-1.4 dB). The lower half of Table 1 examines the EEP values necessary to best reproduce the *Morley et al.* [2010b] reported peak riometer observations (ΔCNA obs. of 1.25 dB), and contrasts the ΔVLF calc. predicted for these fluxes. In all cases, despite the different undisturbed ionospheric electron density height profiles and neutral atmospheric parameters, the typical observed ΔCNA is reproduced by an EEP flux magnitude of ~8×10^{5} electrons cm^{-2} sr^{-1} s^{-1}, with relatively small differences in the ΔVLF calc. relative to those observed.

6. Discussion

The >30 keV EEP flux magnitude determined from Table 1 should be contrasted with that found in the SEA of the POES precipitating electrons. The peak in the median >30 keV POES 0º-telescope fluxes is ~7×10^{4} el. cm^{-2}sr^{-1} s^{-1}, with the 95% confidence interval for the median spanning ~4×10^{4} to 1×10^{5} el. cm^{-2}sr^{-1} s^{-1}. Clearly, this is approximately one order of magnitude smaller than the EEP determined in Section 5 from the ground-based measurements. The difference is significant; if the EEP flux was 7×10^{4} el. cm^{-2}sr^{-1} s^{-1}, the riometer absorption change would be only 0.27 dB. It is not unexpected that the POES-reported 0º-telescope flux is a fraction of that in the bounce loss cone and striking the atmosphere. As noted in section 2.2, the POES SEM-2 0º-telescope only samples a fraction of the loss cone, with 10% being a common "best case".

Note that the typical SWSI-triggered >30 keV electron precipitation flux of 8×10^{5} electrons cm^{-2} sr^{-1} s^{-1} determined from the ground-based instruments should be considered a large electron precipitation event, although with a softer energy spectra than the k=-2 spectra reported as typical by *Clilverd et al.* [2010]. A >30 keV precipitation flux of 2.2×10^{6} electrons cm^{-2}sr^{-1}s^{-1} would occur if the entire electron flux stored in a L=6.5 fluxtube was precipitated out in a 10 minute period, with the population calculated using the ESA-SEE1 radiation belt model [*Vampola*, 1996]. In practice the POES observations indicate that SWSI-triggered geomagnetic storm have roughly constant precipitation fluxes with values similar to those of the peak level for ~1.5 days. We speculate that this is evidence that the acceleration process which "rebuilds" the energetic electron fluxes after the dropout also produces electron precipitation, with a significant fraction of the accelerated electrons being lost into the atmosphere.

7. Summary and Conclusions

In this study we have we examined satellite and ground-based observations to describe the significance of energetic electron precipitation during SWSI-driven geomagnetic storms, focusing on the *Morley et al.* [2010b] epochs to allow "like with like" comparisons with the earlier study focused primarily upon GPS observations. Superposed Epoch Analysis of the low-Earth orbiting POES satellite observations confirm that SWSI-driven geomagnetic storms are strongly associated with large EEP events. However, the EEP only becomes significant at the time that the dropout is at its deepest point and is starting to recover, such that EEP cannot be used to explain the observed dropouts in trapped energetic radiation belt electrons for any energy range. Our observations are more suggestive of the opposite phenomena, where the EEP is the signature of wave-particle driven acceleration processes which serve to reverse the electron flux dropouts.

Previous studies have suggested that magnetopause shadowing may be the primary reason for the rapid dropouts. Our Superposed Epoch Analysis is, however, not consistent with a simple model of direct magnetopause shadowing causing the losses. In particular, we found that the trapped proton fluxes increased rather than decreased during the dropouts, while the classic direct magnetopause shadowing explanation would predict this mechanism would be independent of particle charge, mass or energy, such that electrons or protons which are drifting around the Earth on the same L-shell (but in opposite directions) will encounter the magnetopause and hence be lost.

Ground-based observation of subionospheric VLF propagation from the AARDDVARK network has been used to confirm the POES observations of large EEP events generated by the SWSI-triggered storms. For the epochs for which there were data available and well defined QDCs, 74% of the Morley epochs showed evidence of EEP occurring, producing amplitude changes of several decibels. The EEP was observed typically ~3 hours after the Morley epochs. The AARDDVARK observations were combined with riometers measurements made for the *Morley et al.* [2010b] epochs in order to model the magnitude of the EEP occurring in these events. The very high levels of agreement in the modeling, which involved multiple instruments, and multiple transmitter-receiver paths, indicates a strong probability that the >30 keV EEP flux magnitude has a value close to 8×10^5 electrons $cm^{-2}\ sr^{-1}\ s^{-1}$. This is ~11 times larger than the >30 keV EEP flux reported by the 0º-directed >30 keV electron telescope measurements made onboard POES, which is expected as the POES telescopes only view ~10% of the bounce loss cone.

Acknowledgments. ATH, CJR, MAC, and NRT were supported by the New Zealand Marsden Fund. The research leading to these results has also received funding from the European Union Seventh Framework Programme [FP7/2007-2013] under grant agreement n°263218.

References

Clilverd, M. A., T. D. G. Clark, A. J. Smith, and N. R. Thomson (1993), Observation of a decrease in midlatitude whistler-mode signal occurrence prior to geomagnetic storms, *J. Atmos. Terr. Phys.*, 55, 1479 – 1485, doi:10.1016/0021-9169(93)90113-D.

Clilverd, M. A., C. J. Rodger, N. R. Thomson, J. B. Brundell, Th. Ulich, J. Lichtenberger, N. Cobbett, A. B. Collier, F. W. Menk, A. Seppälä, P. T. Verronen, and E. Turunen (2009), Remote sensing space weather events: the AARDDVARK network, *Space Weather*, 7, S04001, doi: doi:10.1029/2008SW000412.

Clilverd, M. A., C. J. Rodger, R. J. Gamble, Th. Ulich, T. Raita, A. Seppälä, J. C. Green, N. R. Thomson, J. A. Sauvaud, and M. Parrot (2010), Ground-based estimates of outer radiation belt energetic electron precipitation fluxes into the atmosphere, *J. Geophys. Res.*, 115, A12304, doi:10.1029/2010JA015638.

Green, J. C., T. G. Onsager, T. P. O'Brien, and D. N. Baker (2004), Testing loss mechanisms capable of rapidly depleting relativistic electron flux in the Earth's outer radiation belt, *J. Geophys. Res.*, 109, A12211, doi:10.1029/2004JA010579.

Evans, D. S., and M. S. Greer (2004), Polar Orbiting environmental satellite space environment monitor - 2 instrument descriptions and archive data documentation, NOAA technical Memorandum version 1.4, Space Environment Laboratory, Colorado.

Hess, W. N. (1968), The radiation belt and magnetosphere, Blaisdell Pub. London.

Lam, M. M., R. B. Horne, N. P. Meredith, S. A. Glauert, T. Moffat-Griffin, and J. C. Green (2010), Origin of energetic electron precipitation >30 keV into the atmosphere, *J. Geophys. Res.*, 115, A00F08, doi:10.1029/2009JA014619.

Loewe, C. A., and G. W. Prölss (1997), Classification and mean behavior of magnetic storms, *J. Geophys. Res.*, 102(A7), 14,209–14,213, doi:10.1029/96JA04020.

Meredith, N. P., R. B. Horne, M. M. Lam, M. H. Denton, J. E. Borovsky, and J. C. Green (2011), Energetic electron precipitation during high-speed solar wind stream driven storms, *J. Geophys. Res.*, 116, A05223, doi:10.1029/2010JA016293.

Miyoshi, Y., and R. Kataoka (2008), Flux enhancement of the outer radiation belt electrons after the arrival of stream interaction regions, *J. Geophys. Res.*, 113, A03S09, doi:10.1029/2007JA012506.

Morley, S. K., R. H. W. Friedel, T. E. Cayton, and E. Noveroske (2010a), A rapid, global and prolonged electron radiation belt dropout observed with the Global Positioning System constellation, *Geophys. Res. Lett.*, 37, L06102, doi:10.1029/2010GL042772.

Morley, S. K., R. H. W. Friedel, E. L. Spanswick, G. D. Reeves, J. T. Steinberg, J. Koller, T. Cayton, and E. Noveroske (2010b), Dropouts of the outer electron radiation belt in response to solar wind stream interfaces: global positioning system observations, *Proc. R. Soc. A*, 466(2123), 3329, doi:10.1098/rspa.2010.0078.

Newnham, D. A., P. J. Espy, M. A. Clilverd, C. J. Rodger, A. Seppälä, D. J. Maxfield, P. Hartogh, K. Holmén, and R. B. Horne (2011), Direct observations of nitric oxide produced by energetic electron precipitation in the Antarctic middle atmosphere, *Geophys. Res. Lett.*, 38(20), L20104, doi:10.1029/2011GL049199.

O'Brien, T. P., R. L. McPherron, D. Sornette, G. D. Reeves, R. Friedel, and H. J. Singer (2001), Which magnetic storms produce relativistic electrons at geosynchronous orbit?, J. Geophys. Res., 106, 15,533–15,544.

Reeves, G. D., et al., (2003), Acceleration and loss of relativistic electrons during geomagnetic storms, *Geophys. Res. Lett.*, vol. 30(10), 1529, doi:10.1029/2002GL016513.

Roederer, J. G. (1970), Dynamics of Geomagnetically Trapped Radiation, 413 Springer, New York.

Rodger, C. J., M. A. Clilverd, N. R. Thomson, R. J. Gamble, A. Seppälä, E. Turunen, N. P. Meredith, M. Parrot, J. A. Sauvaud, and J.-J. Berthelier (2007), Radiation belt electron precipitation into the atmosphere: recovery from a geomagnetic storm, *J. Geophys. Res.*, 112, A11307, doi:10.1029/2007JA012383.

Rodger, C. J., M. A. Clilverd, J. Green, and M.-M. Lam (2010a), Use of POES SEM-2 observations to examine radiation belt dynamics and energetic electron precipitation in to the atmosphere, *J. Geophys. Res.*, 115, A04202, doi: 10.1029/2008JA014023.

Rodger, C. J., B. R. Carson, S. A. Cummer, R. J. Gamble, M. A. Clilverd, J-A. Sauvaud, M. Parrot, J. C. Green, and J.-J. Berthelier (2010b), Contrasting the efficiency of radiation belt losses caused by ducted and non-ducted whistler mode waves from ground-based transmitters, *J. Geophys. Res.*, 115, A12208, doi:10.1029/2010JA015880.

Rodger, C. J., M. A. Clilverd, A. J., Kavanagh, C. E. J. Watt, and P. T. Verronen (2012), Contrasting the responses of three different ground-based instruments to energetic electron precipitation, *Radio Sci.*., 47, RS2021, doi:10.1029/2011RS004971.

Sandanger, M., F. Søraas, K. Aarsnes, K. Oksavik, and D. S. Evans (2007), Loss of relativistic electrons: Evidence for pitch angle scattering by electromagnetic ion cyclotron waves excited by unstable ring current protons, *J. Geophys. Res.*, 112, A12213, doi:10.1029/2006JA012138.

Seppälä, A., C. E. Randall, M. A. Clilverd, E. Rozanov, and C. J. Rodger (2009), Geomagnetic activity and polar surface level air temperature variability, *J. Geophys. Res.*, 114, A10312, doi:10.1029/2008JA014029.

Thomson, N. R., C. J. Rodger, and M. A. Clilverd (2011), Daytime D-region Parameters from Long Path VLF Phase and Amplitude, *J. Geophys. Res.*, 116, A11305, doi:10.1029/2011JA016910.

Thorne, R. M. (2010), Radiation belt dynamics: The importance of wave-particle interactions, *Geophys. Res. Lett.*, 37, L22107, doi:10.1029/2010GL044990.

Turner, D. L., S.K. Morley, Y. Miyoshi, B. Ni, and C.-L. Huang, Outer radiation belt flux dropouts: Current understanding and unresolved questions, *American Geophysical Union Monograph on "Dynamics of the Earth's Radiation Belts and Inner Magnetosphere"* edited by D. Summers, I. R. Mann, D. N. Baker, and M. Schulz (in preparation), 2012.

Turunen, E., P T Verronen, A Seppälä, C J Rodger, M A Clilverd, J Tamminen, C F Enell and Th Ulich (2009), Impact of different energies of precipitating particles on NOx generation in the middle and upper atmosphere during geomagnetic storms, *J. Atmos. Sol. Terr. Phys.*, 71, pp. 1176-1189, doi:10.1016/j.jastp.2008.07.005

Vampola A.L. (1996), Outer Zone Energetic Electron Environment Update, European Space Agency P.O. #151351.

Van Allen, J. A. and L. A. Frank (1959), Radiation Measurements to 658,300 Kilometers with Pioneer IV, *Nature*, 184, 219-224.

Yando, K., R. M. Millan, J. C. Green, and D. S. Evans (2011), A Monte Carlo simulation of the NOAA POES Medium Energy Proton and Electron Detector instrument, *J. Geophys. Res.*, 116, A10231, doi:10.1029/2011JA016671.

M. A. Clilverd, British Antarctic Survey, High Cross, Madingley Road, Cambridge CB3 0ET, England, U.K. (e-mail: macl@bas.ac.uk).

A. T. Hendry, C. J. Rodger, and N. R. Thomson, Department of Physics, University of Otago, P.O. Box 56, Dunedin, New Zealand. (email: ahendry@physics.otago.ac.nz, crodger@physics.otago.ac.nz, n_thomson@physics.otago.ac.nz).

S. K. Morley, Los Alamos National Laboratory, Bikini Atoll Road, SM 30, Los Alamos, NM 87545, USA. (smorley@lanl.gov)

T. Raita, Sodankylä Geophysical Observatory, University of Oulu, Sodankylä, Finland. (email: tero.raita@sgo.fi)

HENDRY ET AL.: RAPID RADIATION BELT LOSSES

Tables

	ΔVLF obs.	ΔVLF calc.	ΔCNA calc.	EEP flux
NAA-CHUR	+2.0 dB	+2.0 dB	1.41 dB	1×10^6
GVT-SGO	-1.5 dB	-1.1 dB	1.05 dB	4×10^5
NAA-SGO	+2.5 dB	+2.5 dB	1.35 dB	9×10^5
	ΔCNA obs.	**ΔVLF calc.**	**ΔCNA calc.**	**EEP flux**
NAA-CHUR	1.25 dB	+1.7 dB	1.25 dB	8×10^5
GVT-SGO	1.25 dB	-0.9 dB	1.25 dB	8×10^5
NAA-SGO	1.25 dB	+2.4 dB	1.25 dB	8×10^5

Table 1. Summary of ground-based instrument responses during the SWSI-triggered geomagnetic storms. The top half of the table examines the EEP values necessary to best reproduce the subionospheric VLF observations from this study (ΔVLF obs.), while the lower half examines the EEP values necessary to best reproduce the *Morley et al.* [2010b]-reported riometer observations (ΔCNA obs.). In each case the calculated change of the other ground-based instrument response is shown. The EEP values listed are >30 keV electron fluxes with units of electrons cm^{-2} sr^{-1} s^{-1}.

Figures

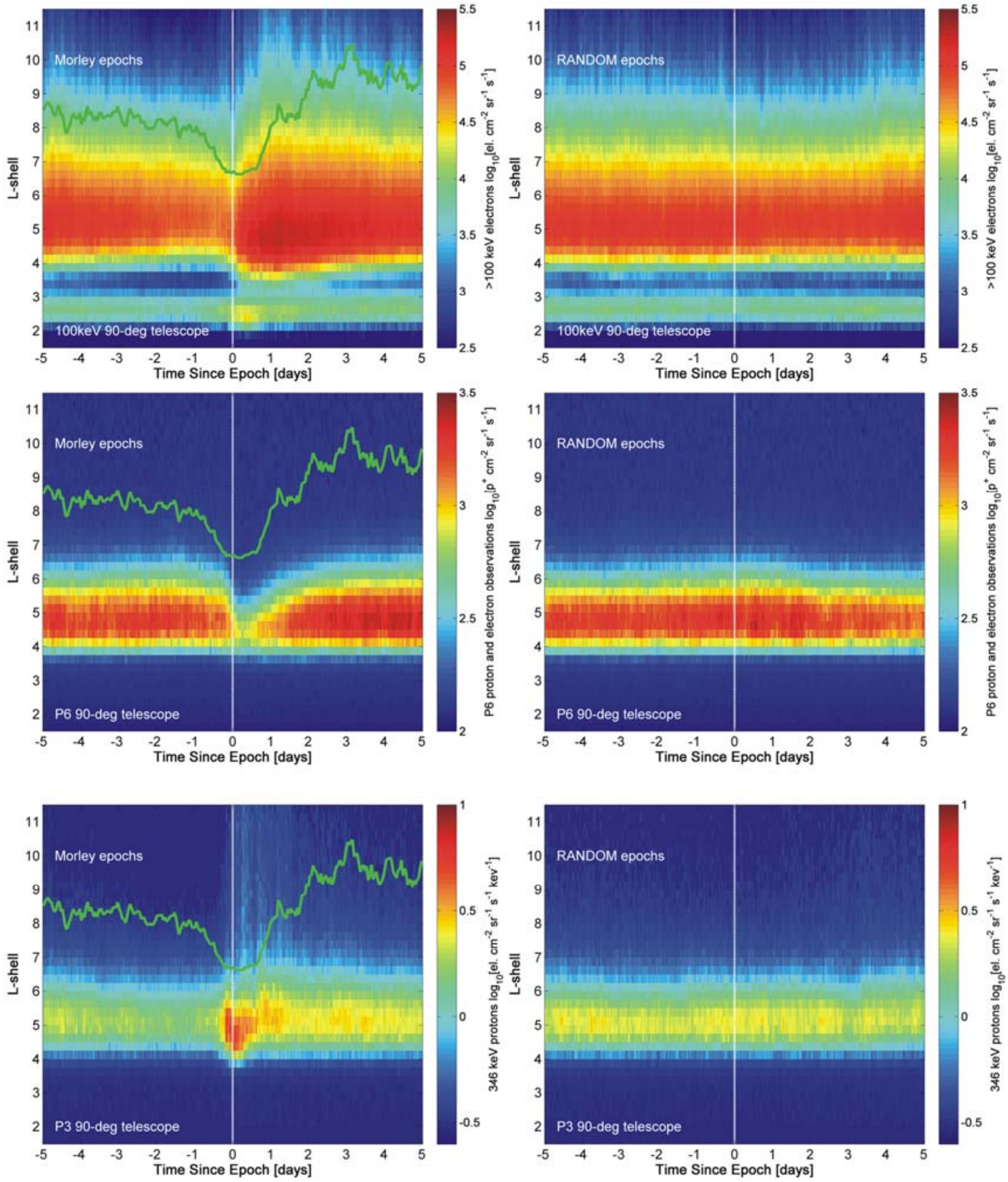

Figure 1. Superposed epoch analysis undertaken using the POES MEPED data. The left hand panels show the analysis applied to 65 of the *Morley et al.* [2010b] epochs, while the right hand panels are for a set of random epochs. The upper panels are the integral flux observations from the >100 keV 90º telescope, the middle panels show counts from the P6 90º telescope (which responds to relativistic electrons), and the lower panels the differential protonflux at 346 keV from the P3 90º telescope. As a guide to the eye, all of the left hand

panels have the result of the Morley superposed epoch analysis applied to GOES >600 keV trapped flux observations (green line).

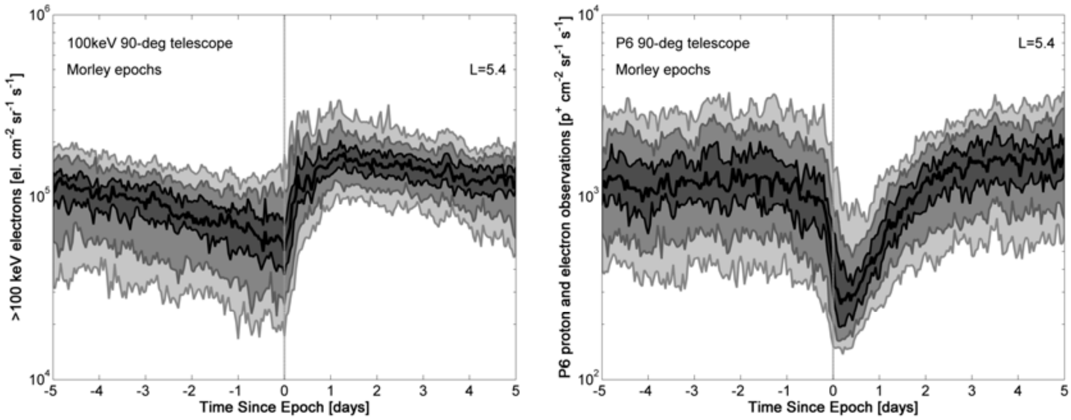

Figure 2. Superposed epoch analysis of the POES 90º telescope >100 keV and P6-measured relativistic trapped electron fluxes at *L*=5.4. The superposed epoch median of the quantity is given by a black line. The 95% confidence interval for the median is given by the dark grey band. The mid- grey bands mark the interquartile range and the 95% confidence interval about it (light grey).

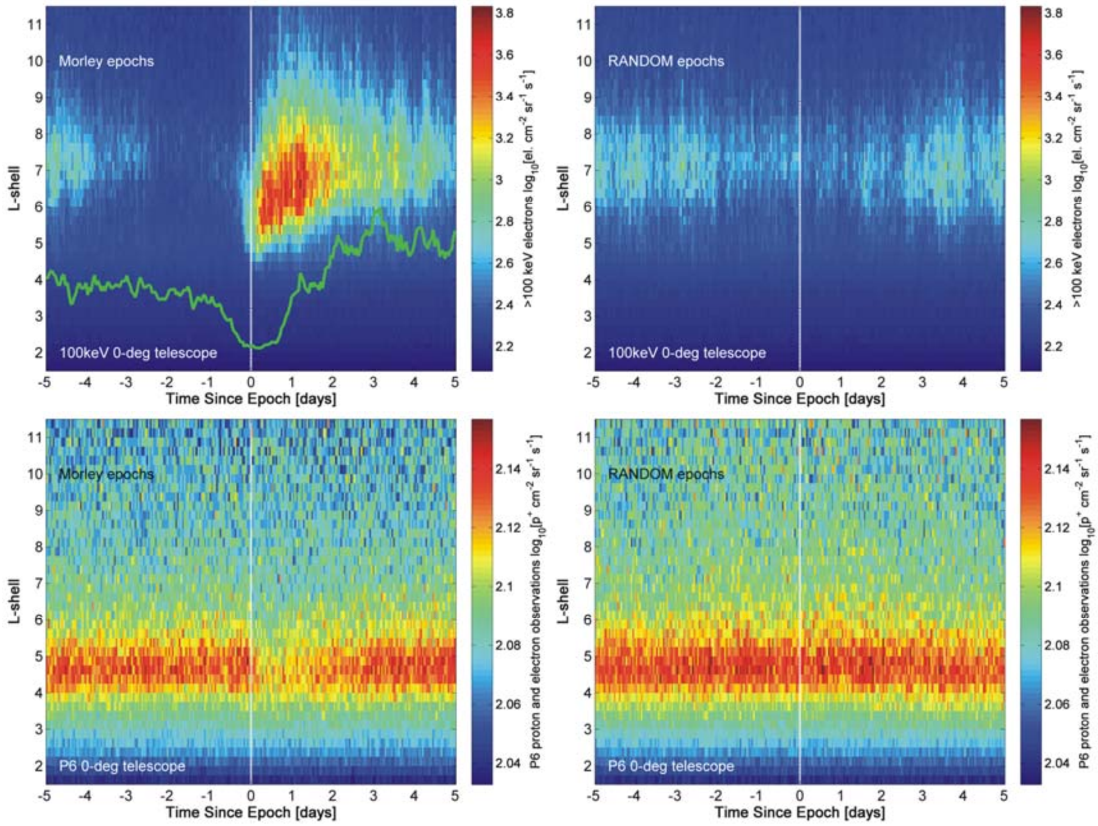

Figure 3. Superposed epoch analysis of 0º directed MEPED telescopes in the same format as Figure 1. The upper panels are the integral flux observations from the >100 keV 0º telescope, while the lower panels show counts from the P6 0º telescope (which responds to relativistic electrons).

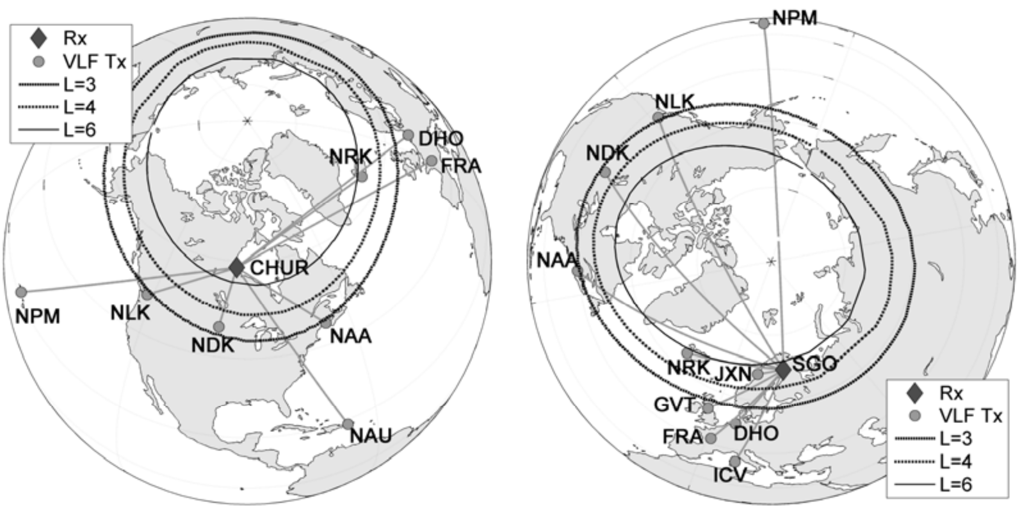

Figure 4. Map showing the AARDDVARK receivers at Churchill and Sodankylä (diamonds) and the VLF transmitters monitored by these receivers (circles). This map also indicates the great circle propagation paths between the transmitter and receiver, as well as a number of fixed *L*-shell contours evaluated at 100 km altitude.

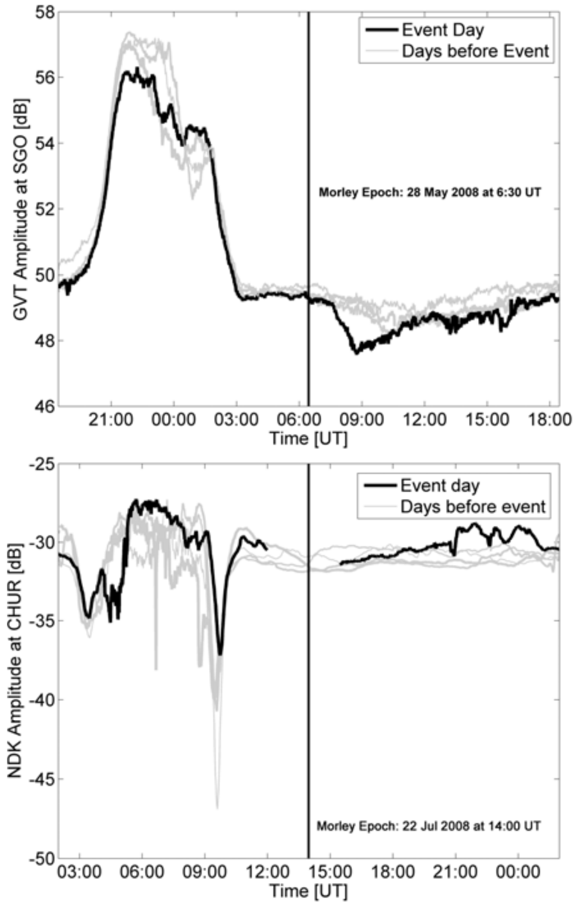

Figure 5. Examples of AARDDVARK observations made around the time of the Morley epochs (the epoch time is marked by the vertical lines in the centre of the plots. Observations on the days before the epoch day are plotted in grey, the epoch day in black. The upper panel shows GVT-Sodankylä amplitudes for the epoch at 6:30 UT on 28 May 2008, while the lower panel shows NDK-Churchill amplitudes for the epoch at 14:00 UT on 22 July 2008.